catalysts

MDPI

Article

Pristine TiO_2 and Sr-Doped TiO_2 Nanostructures for Enhanced Photocatalytic and Electrocatalytic Water Splitting Applications

Mohd Fazil and Tokeer Ahmad *

Nanochemistry Laboratory, Department of Chemistry, Jamia Millia Islamia, New Delhi 110025, India; fazilzeus@gmail.com

* Correspondence: tahmad3@jmi.ac.in; Tel.: +91-11-26981717 (ext. 3261)

Abstract: Pristine TiO_2 and Sr-doped TiO_2 (1%, 2.5% and 5%) nanoparticles were synthesized at low temperatures via an eco-friendly hydrothermal route for water-splitting applications. XRD, EDAX and Raman analysis were performed to analyze the crystallinity, purity and structure of the as-synthesized materials. TEM, SEM, BET and UV-DRS studies were carried out to elucidate the size, morphology, surface area and optoelectronic properties of the nanoparticles. High surface areas of 169, 182, 178 and 141.16 $m^2\ g^{-1}$ for pristine TiO_2 (12 $\pm$ 0.6 nm) and 1% (11.1 $\pm$ 0.6 nm), 2.5% (12.1 $\pm$ 0.6 nm) and 5% (13 $\pm$ 0.7 nm) Sr-doped TiO_2 nanoparticles were obtained, respectively. One-percent Sr-doped TiO_2 nanoparticles were found to be active photocatalysts, as they showed higher hydrogen production (26.30 mmolg_{cat}^{-1}). Furthermore, electrocatalysis was investigated for HER and OER in 0.5 N H_2SO_4 and 0.1 N KOH electrolytic solutions using calomel as a reference electrode, revealing that 1% and 5% Sr-doped TiO_2 showed maximum current density for both HER ($\approx$10 mA/cm^2) and OER ($\approx$2.49 mA/cm^2), with an onset potential of 0.96 V for HER and 1.55 V for OER, and Tafel slopes of 84.09 and 91.60 mV/dec, respectively.

Keywords: Sr-doped TiO_2 nanoparticles; hydrothermal synthesis; photocatalysis; electrocatalysis; water splitting; hydrogen energy

Citation: Fazil, M.; Ahmad, T. Pristine TiO_2 and Sr-Doped TiO_2 Nanostructures for Enhanced Photocatalytic and Electrocatalytic Water Splitting Applications. *Catalysts* **2023**, *13*, 93. https://doi.org/10.3390/catal13010093

Academic Editors: Jaime Carbajo and Patricia García-Muñoz

Received: 6 November 2022
Revised: 15 December 2022
Accepted: 26 December 2022
Published: 2 January 2023

1. Introduction

Hydrogen production through photocatalytic water splitting is considered to be the most renewable and sustainable energy production technology, with almost negligible impact on the environment [1]. Hydrogen is considered to be the most promising and clean source of energy for the future, as the only combustion product is water. Furthermore, with the process of development, the demand for energy is also increasing. As a result, present energy resources cannot last long and fulfill our future requirements. Advanced functional nanomaterials have shown potential applications in nanocatalysis for H_2 generation to meet the global energy demand [2–4]. The utilization of non-renewable energy resources has become one of the major causes of environmental pollution due to the release of CO_2, which causes the greenhouse effect and global warming [5–8]. Hence, the researchers are trying to develop sustainable and environment-friendly energy resources with high gravimetric energy density that are easily accessible. There are several environment-friendly techniques for green fuel/energy on which researchers are working; among them, photo- and electrocatalytic techniques have attracted significant attention -due to their relatively decreased dangers to the environment [2,4,5,9–11]. In today's era, hydrogen energy has become the center of attraction, and water-splitting via electro-catalysis or photo-catalysis is considered to be the best method for hydrogen generation, presenting a clean and renewable source of energy for fuel cells and batteries [12]. To store renewable electricity, electrochemical water-splitting is one of the most attractive ways of achieving hydrogen energy [13]. Nanosized metal oxide nanoparticles are widely used in the semiconductor industry as catalysts for hydrogen generation due to their low toxicity, high stability and low cost [14,15].

Transition metal-based oxides have wide band gap semiconducting properties, which are large enough for water splitting and charge transfer. This meets the thermodynamic requirement, showing excellent hydrogen evolution performance as photo- and electrocatalysts because of their exceptional size dependency [16,17]. These materials have extraordinary optoelectronic and chemical properties, along with advanced chemical and thermal stabilities with these processes encompassing charge carrier (e^-/h^+) transformation [18–21]. Recently, several metals and non-metal oxide-based catalysts have been explored as photo- and electrocatalysts for significant hydrogen evolution activity [22–29]. The use of metal oxides as catalysts was uncovered by the use of TiO_2 as a catalyst in photocatalytic and electrocatalytic water splitting. Honda and Fujishima (in 1972) used TiO_2 with a Pt electrode for the electrocatalysis of water [30]. However, it has very limited application as a photocatalyst, though due to it low cost, non-toxicity and excellent physical and chemical properties, TiO_2 was found to be very useful in the paint industry, cosmetics industry, gas sensors, optoelectronic devices, protective coating, white pigment, catalysis and electronics, etc [16,17,31–35].

The photocatalysis mechanism is based on e^- and h^+ pair formation with the irradiation of a light source [36–39]. Due to wide bandgap (3.2 eV) energy, fast charge carrier recombination rate, and low utilization of lights, the photocatalytic activity of TiO_2 towards hydrogen evolution is limited [36,38]. To overcome these issues, researchers have tried to develop TiO_2 materials to reduce the band gap and charge separation enhancement in many ways, such as by coupling it with other semiconductors and doping with foreign elements [40]. Metal doping to TiO_2 host lattice causes surface plasmon resonance (SPR), which is free electrons on the metal-doped nano-catalyst. Owing to SPR, the charge transfer efficiency of metal-doped TiO_2 is enhanced through electron trapping via efficient absorption of solar radiation [41,42]. In addition, metal doping introduces interstitial site defects and oxygen vacancies by the formation of Ti^{3+} in the TiO_2 lattice. Furthermore, metal doping and heterostructured composites create an empty impurity band above the valence band (V.B.) and bridge most of the gaps of valence band maxima and conduction band (C.B.) minima in pristine TiO_2, with less charge (e^-/h^+) separation and charge transfer. This leads to the tailoring of the bandgap and hence enhances the photo- and electrocatalytic performance of the nanocatalysts [43–46]. For instance, iron, cobalt, molybdenum, strontium, magnesium or noble metals (Ag, Pt, Au) and non-metal elements (C, N, S) have been exploited as dopants to improve the photocatalytic and electrocatalytic performance of pristine TiO_2 [47–50]. Strontium is a significant alkaline earth metal extensively used in many research fields, electronics, the military industry, the chemical industry, optics, metallurgy, etc. In recently reported literature related to Sr and TiO_2 systems, most researchers reported Sr-doped composite materials or nanostructures. Film Sr-doped TiO_2 nanotube shows a 65% incident photon conversion efficiency. Sr-doping to TiO_2 enhances the visible light response and generates active site defects in the pristine TiO_2 host lattice; it thereby enhances the activity by a decrease in the band gap and suppresses the charge recombination rate [49,51]. The precious nature of metals (Ru, Ir, W, etc.) and oxides, which are the most efficient electro-active materials for OER, is becoming a bottleneck for commercial applications [52–55]. Since OER follows a complex multistep reaction mechanism, it involves four electrons in either an acidic or alkaline medium (OER, $2H_2O \rightarrow O_2 + 4H^+ + 4e^-$ in acidic solution, $4OH^- \rightarrow O_2 + 2H_2O + 4e^-$ in alkaline solution); hence, OER reactions have high overpotential and sluggish kinetics even after using active electrocatalysts such as RuO_2 and IrO_2, which is hinders practical application of water electrocatalysis [56–58]. For OER, RuO_2 and IrO_2 are considered the best electrocatalysts owing to their high stability, excellent electrolytic activity and low overpotential [59,60].

The major concern of the current research is to develop highly efficient, cheap and earth-abundant electrocatalysts and photocatalysts for use in sustainable energy. Herein, we report a simple, environmentally friendly, low-temperature hydrothermal approach to the synthesis of pristine and Sr-doped TiO_2 nanocatalysts. As-synthesized material was further investigated with XRD, Raman, TEM, SEM, EDX, BET and UV-vis DRS. In

addition, detailed photo and electrocatalytic water-splitting studies were carried out for the application of as-prepared Sr-doped TiO_2 nanoparticles for hydrogen production.

2. Experimental Section

2.1. Materials

The following chemicals and reagents were used without further purification: glacial acetic acid (Fisher Scientific, Heysham, Lancashire, UK), titanium isopropoxide (Alfa Aesar, 97%, Heysham, Lancashire, UK), sodium hydroxide (97%, Merck Life Science Pvt. Ltd., Vikhroli, Mumbai, India), strontium acetate (Aldrich, Sigma-Aldrich Chemie GmbH, Steinheim, Germany), ethanol (Merck, 99.9%, Darmstadt, Germany), sodium sulfide (Na_2S, 60%, SRL Pvt. Ltd., Taloja, Maharashtra, India), sodium sulfite (Na_2SO_3, Alfa Aesar, 98%, Heysham, England), and double distilled water.

2.2. Synthesis of Pristine and Sr-Doped TiO_2 Nanoparticles (NPs)

Pristine TiO_2 NPs were synthesized through a hydrothermal route using a laboratory autoclave. 7.4 mL glacial acetic acid was taken in a round-bottom flask to prevent the direct oxidation of titanium isopropoxide to TiO_2, which helps to carry out the reaction in a controlled manner by forming stable hydroxyl titanium acylate [61,62]; then, 0.74 mL of titanium isopropoxide was added after making an inert atmosphere with continuous stirring. After, 16.86 mL of distilled water was added such that the total volume became 25 mL; the resulting solution is referred to as 0.1 M Ti^{4+} [61,62]. This solution was stirred on a magnetic stirrer for about 30 min with slow addition of 25 mL of 0.1 M NaOH. The solution was then kept in an autoclave and placed in a vacuum oven at 150 °C for 12 h. The solution was cooled to room temperature and then centrifuged, washed with distilled water and ethanol several times, and dried overnight at 60 °C. Then, the dried white precipitate was ground and white powders were obtained.

For the preparation of three different compositions, 25 mL of strontium acetate solution of 0.001 M was prepared by doping 1.0% of strontium in 0.1 M of TiO_2. In addition, a solution of titanium metal ions was prepared using a similar procedure to that stated above. These two solutions were mixed and stirred on a magnetic stirrer with slow addition of 45 mL of 0.1 M NaOH solution for about 30 min [29], followed by a normal synthesis procedure to obtain washed and dried precipitate, which was ground to obtain a white-yellowish powder. Similarly, the procedure for the doping of 2.5% and 5.0% of Sr in TiO_2 nanoparticles was performed separately with 0.0025 M strontium acetate solution for 2.5% doping and 0.005 M for 5.0% doping of Sr in TiO_2 nanoparticles. The reaction scheme was depicted schematically in Figure 1 below.

2.3. Characterizations

The powder X-ray diffraction (XRD) technique was employed to analyze the crystal structure and phase purity of the as-prepared samples by employing a Rigaku Japan D/max 2500 diffractometer operating at a scan rate of 5° min^{-1} with Cu Kα radiation (1.5406 Å) with a step size of 0.05 °/s to carry out the XRD studies in the 2θ range of 20–80°. A RENISHAW inVia Raman microscope (Leica Microsystems CMS GmbH, Wetzlar, Germany) with a He–Ne laser and an output of 15 mW was used to analyze the Raman spectral studies using a 532 nm excitation wavelength. TEM analyses were carried out on a TALOS instrument operating at 200 kV to investigate the size and crystal structure of undoped pristine and Sr-doped TiO_2 nanoparticles. The samples for TEM analysis were prepared by making creating a suspension in ethanol by sonication and mounting the samples on a carbon-coated copper grid by employing a droplet of suspension. A Nova Nano SEM-450 microscope (FEI Company, Hillsboro, OR, USA) accelerated at 20 kV voltage combined with an energy-dispersive X-ray (EDAX) system was used to perform field emission scanning electron microscopy (FESEM) to evaluate the surface morphological features, elemental analysis and chemical composition. To analyze the FESEM analysis, a dry sample was mounted on an ultrathin layer of gold coated with carbon tape to prevent the surface

charging effect. UV-visible DRS (UV-Vis diffused reflectance spectroscopy) studies were performed on PerkinElmer Lambda 365 spectrophotometer. The reflectance spectra of as-synthesized samples were recorded in the 200–800 nm wavelength range to determine the band gap. Furthermore, a Nova 2000e Instrument (Quantachrome Instruments Limited, USA) was used to determine the Brunauer–Emmett–Teller (BET) surface area and pore size distribution of pristine TiO_2 and Sr-doped TiO_2 nanoparticles.

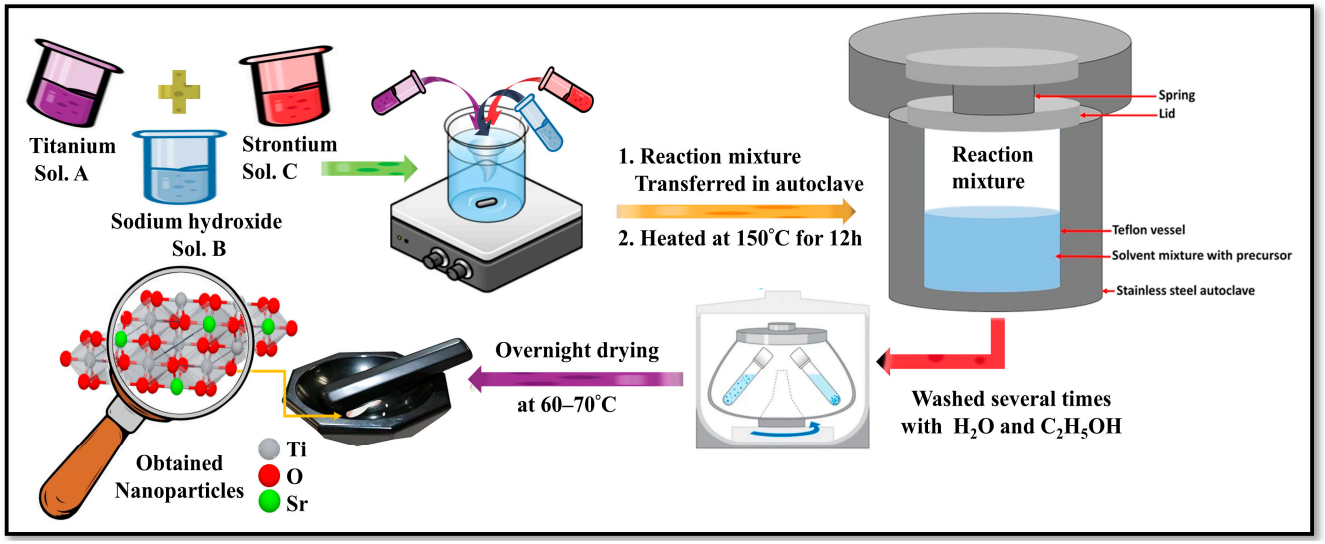

Figure 1. The schematic diagram for the preparation of Sr−doped TiO_2 nanoparticles.

2.4. Photocatalytic Hydrogen Evolution Measurements

The activity of the as-synthesized nanocatalyst towards photocatalysis of water for hydrogen production was estimated with 0.128 M Na_2S (500 mg) and 0.079 M Na_2SO_3 (500 mg) as sacrificial agents, which provide electron donor sites throughout photocatalytic reaction in ambient conditions irradiated under a UV visible light source of 200–2400 nm varying wavelength. In the hydrogen evolution activity, 20 mg of photocatalyst and sacrificial agents were dispersed in 50 mL double distilled water in an airtight photoreactor, which is a specialized cylindrical quartz cell with a bottleneck of 4 cm diameter and a flat base [63]. The prepared solution was stirred with the purging of nitrogen for 30 min in order to create an inert atmosphere and to eliminate gas impurities (such as dissolved oxygen). After stirring, the cylindrical quartz cell containing the solution mixture was fixed on the stirrer and its flat surface was placed 7 cm away from the light source; it was then exposed to the light source (200 W, Hg−Xe arc lamp, Newport, MODEL: 66906–200HXF-R15 Ozone-free), which irradiates at 170 W with constant stirring. Hydrogen production was quantified using a gas chromatography instrument procured from Perkin Elmer, model Clarus 590 GC, using a TCD detector and nitrogen as carrier gas, with sampling done after every 1 h time interval with a specialized airtight glass syringe. For further study, the photocatalysts from the reaction mixture were recovered by centrifugation, dried and then analyzed the recyclability, photostability, reusability and photocatalytic response showing maximum H_2 production by taking consecutive three cycles of 8 h long activity.

2.5. Electrode Preparation and Electrocatalytic Measurements

For the measurement of electrocatalytic activity of pristine TiO_2 and 1, 2.5 and 5% Sr-doped TiO_2 nanostructures, all electrochemical measurements were taken with three electrode systems (i.e., working electrode, reference electrode and counter electrode) in 0.5 N H_2SO_4 (98%, Merck) and 0.1 N KOH (85%, Merck) electrolyte solution for hydrogen evolution reaction (HER) and oxygen evolution reaction (OER) activity, respectively. Measurements were performed using an Autolab PGSTAT204 instrument at room temperature. Here, Pt wire and saturated calomel electrode (SCE) were used as counter and reference

electrodes, respectively. The working electrodes of as-synthesized pristine TiO_2 and 1, 2.5 and 5% Sr-doped TiO_2 electrocatalysts for the electrochemical setup were prepared by the coating of catalyst dispersion on pretreated ITO substrates (sheet resistance < 10 ohm/sq, Vritra) of 1 × 1 cm^2 dimension. Before the drop-casting of the dispersion on the substrates, they were cleaned with ethanol (Merck, Emsure), acetone (99.5%, SRL) and isopropanol (99.5%, SRL) for 10 min in each solvent by ultra-sonication. Catalyst dispersions were prepared by making a suspension of 4 mg electrocatalysts, 400 µL isopropanol and 15 µL of Nafion (5 wt %, Alfa Aesar) as a polymer binder. The resulting mixtures were sonicated for about 30 min. 250 µL dispersions were deposited via drop casting on the conducting side (oxide layer side) of ITO substrate and then dried overnight at 60 °C in a vacuum oven, as per the procedure reported elsewhere [64]. For investigation of the electrochemical activity of the as-synthesized nanostructures, cyclic voltammetry (CV) measurements were carried out in the range of 10–100 mV/s, linear sweep voltammetry (LSV) measurements were performed at 100 mV/s and chronoamperometry (CA) measurements were obtained at −0.5 V and 0.5 V for HER and OER, respectively.

3. Results and Discussion

3.1. XRD Analysis

Powder X-ray diffraction was used to identify the phase purity and crystal structure of the as-synthesized nanoparticles. Figure 2 presents the XRD pattern, which was satisfactorily indexed with the anatase phase of TiO_2 with JCPDS card number 71-1167 [65]. It was observed that the synthesized material was pure and highly crystalline. Similarly, the 1%, 2.5% and 5% Sr-doped TiO_2 nanoparticles were indexed with the same anatase phase, as shown in Figure 2. From the XRD, it was observed that there is a slight shift in the peaks after Sr-doping, which shows the incorporation of Sr into the host lattice of TiO_2 nanoparticles. Further, the 2θ values shift to lower values with 1% doping of Sr, which then decrease with 2.5% and 5% doping. In addition, with the increase in Sr concentration in the TiO_2 host lattice, the peak intensity increases; sharpness was also observed, which reflects the increase in overall crystallinity. Since the Sr^{2+} (1.12 Å) ionic radius is much higher than Ti^{4+} (0.605 Å), on substitution, lattice expansions were observed. This also suggests that the solubility limit of Sr^{2+} over the TiO_2 host lattice is not high; hence, Sr-doped TiO_2 nanoparticles were fabricated at small concentrations. Due to the effect of Sr dopant, the crystallinity and crystallite size of Sr-doped TiO_2 were considerably reduced. It also causes the enhancement of point defects such as oxygen vacancy [49]. By using Scherrer's equation, the average crystallite size of all samples was calculated [66] and was found to be 10.21 ± 0.5, 8.92 ± 0.5, 8.99 ± 0.5, and 9.85 ± 0.5 nm for pure TiO_2, 1%, 2.5%, and 5% Sr-doped TiO_2, respectively. The crystal structure of Sr-doped TiO_2 nanoparticles depicting the positions of Sr^{2+} and Ti^{4+} ions is shown in Figure 3.

3.2. TEM Analysis

TEM analysis showed the effect of Sr-doping on TiO_2 nanoparticles. Figure 4a–d presents the micrographs of pristine TiO_2 and Sr-doped TiO_2 nanoparticles. In the TEM micrographs, the appearance of rough cubes with little agglomeration could be seen, along with black spots, showing the appearance of strontium on the TiO_2 host nanoparticles. From the TEM images, particle size histograms were obtained, which revealed the average particle size to be in the range of 5–30 nm and the average particle size to be 12 ± 0.6, 11.1 ± 0.6, 12.1 ± 0.6 and 13 ± 0.7 nm for pristine TiO_2, 1%, 2.5% and 5% Sr-doped TiO_2 nanoparticles, respectively, as shown in Figure 4e–h. It was also observed that with the increase in the Sr concentration, the particle size increases. Furthermore, HRTEM micrographs depict the well-defined lattice fringes separated by the interplaner spacing of 0.35, 0.35, 0.35 and 0.35 nm for the pristine, 1%, 2.5%, and 5% Sr-doped TiO_2 nanoparticles, respectively which correspond to the (101) crystallographic plane of anatase tetragonal TiO_2, as shown in Figure 4i–l.

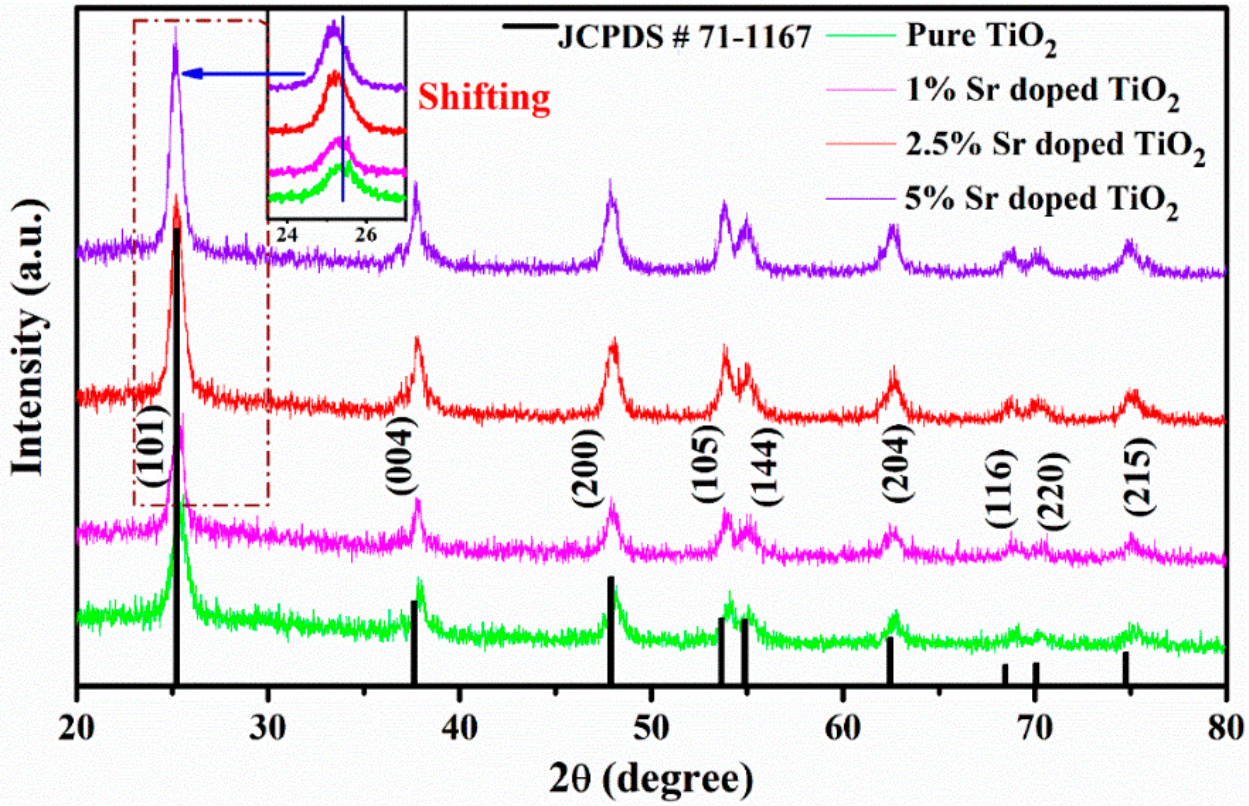

Figure 2. Overlaid XRD patterns of pristine TiO_2, 1%, 2.5% and 5% Sr-doped TiO_2 NPs.

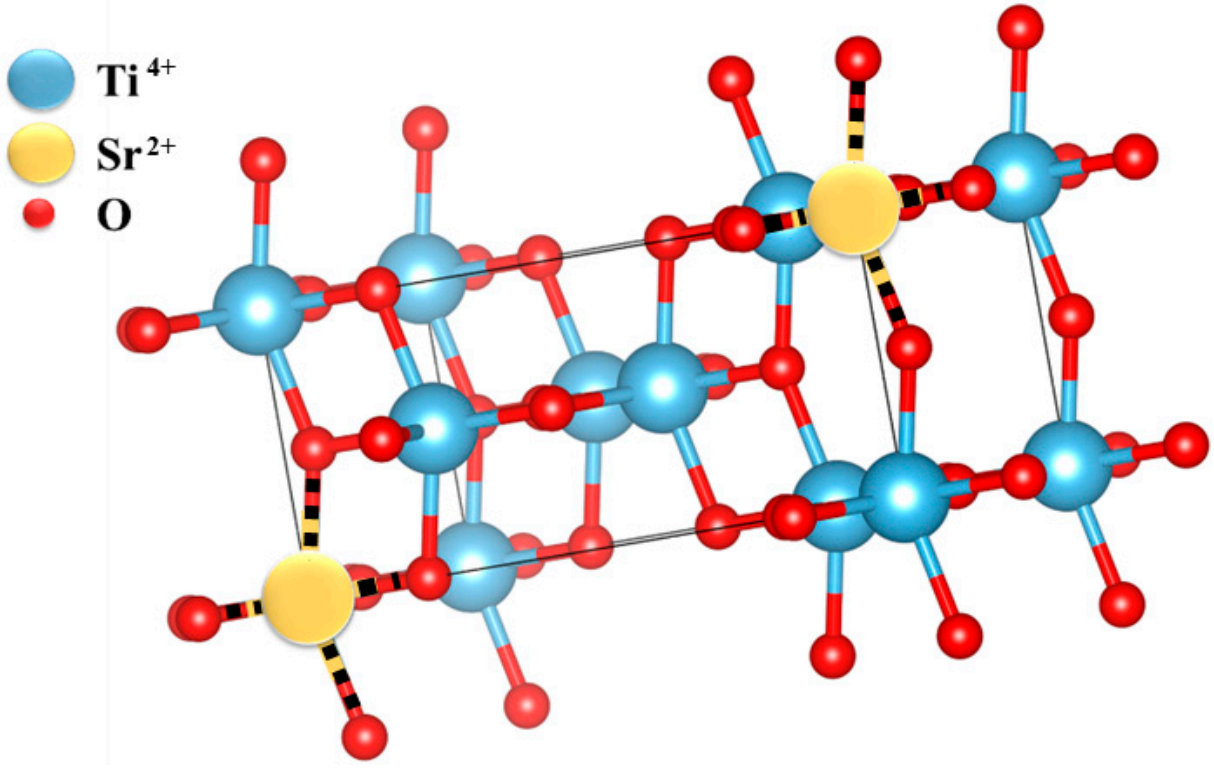

Figure 3. Crystal structure of Sr-doped TiO_2 nanoparticles.

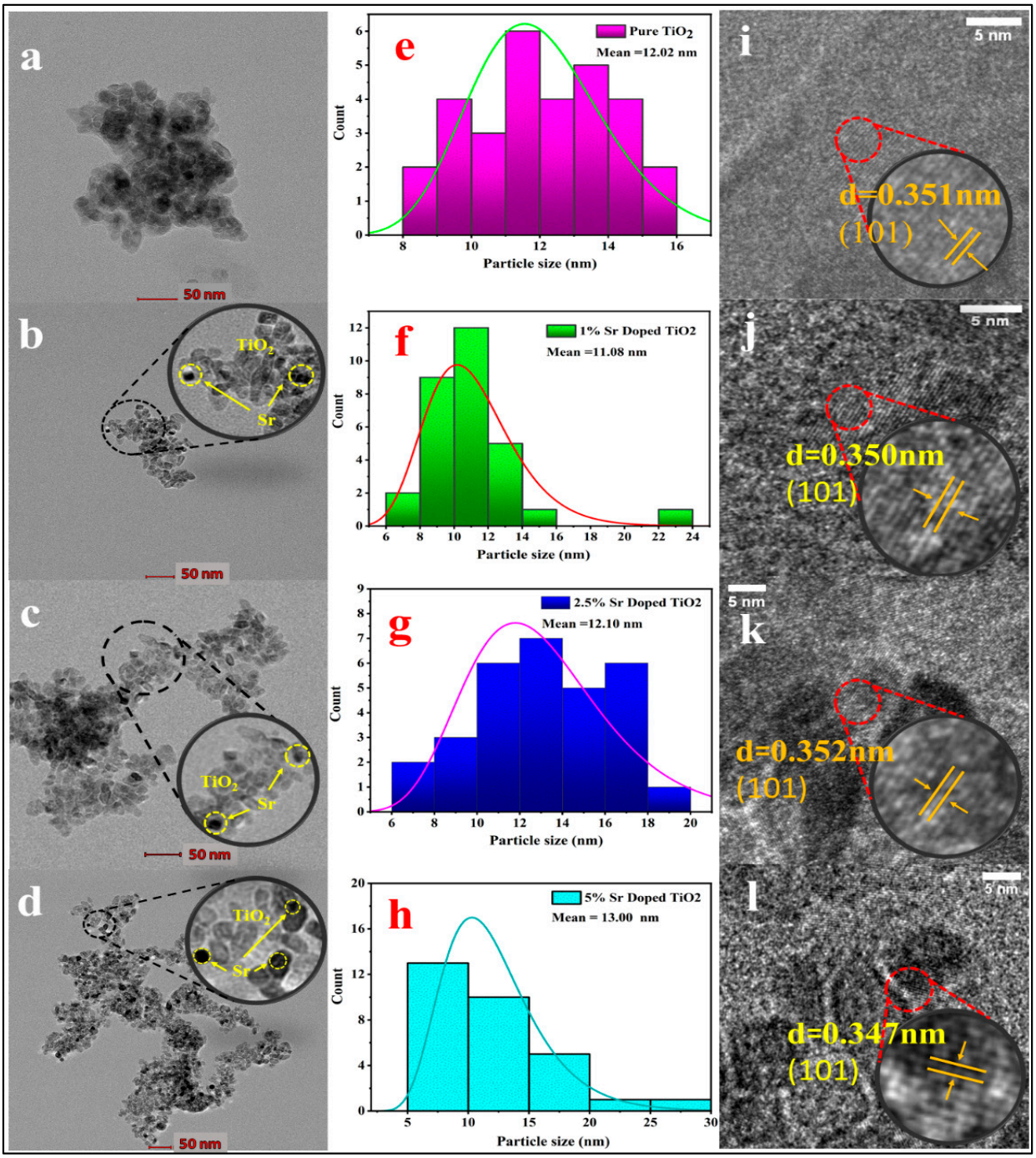

Figure 4. (**a**–**d**) TEM micrographs, (**e**–**h**) size distribution plots and (**i**–**l**) HRTEM micrographs depicting the lattice spacing of the crystallographic planes of pristine TiO_2 and 1%, 2.5% and 5% Sr-doped TiO_2 nanoparticles.

3.3. SEM Analysis

SEM analysis of pristine and Sr-doped TiO_2 nanoparticles was carried out to gather morphological information, as shown in Figure 5a–d. SEM images show the formation of dense nanoparticles with rough and irregular morphology. Careful observation shows that the aggregation and density increase with increasing dopant concentration. The EDAX spectra of pristine TiO_2 and Sr-doped TiO_2 nanoparticles represent the successful doping of Sr into the TiO_2 host lattice, as shown in Figure 5e–h. EDAX spectra show the presence of only the desired elements Sr, Ti and O in the as-synthesized nanoparticles;

theoretically, the derived elemental composition was found to have a close agreement with the experimentally loaded composition. X-ray elemental mapping of pristine TiO_2 and Sr-doped TiO_2 also revealed that Sr was dispersed minutely and Ti and O were present in the synthesized material.

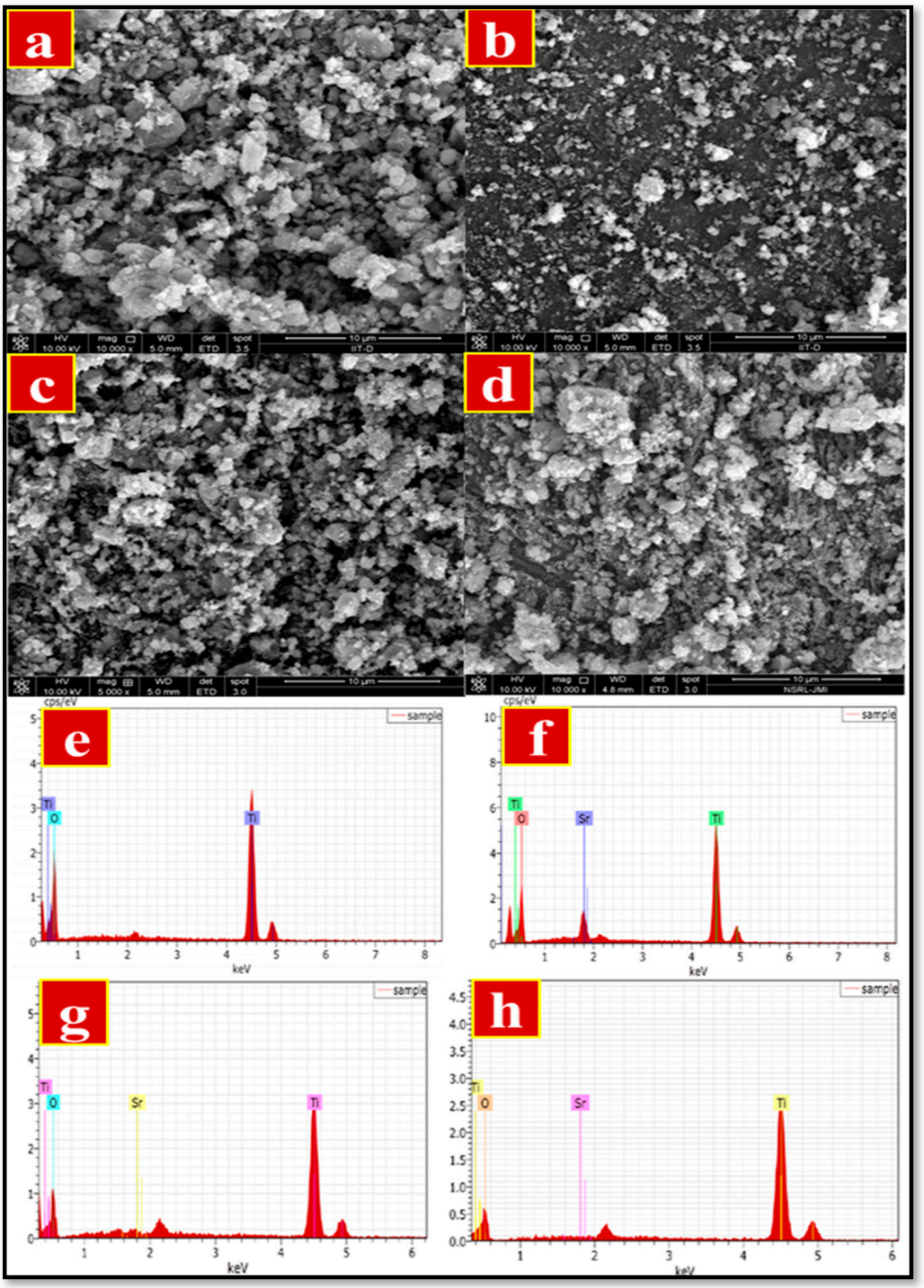

Figure 5. (**a**–**d**) SEM micrographs and (**e**–**h**) EDAX spectra of Pristine TiO_2, 1%, 2.5%and 5% Sr-doped TiO_2 nanoparticles.

3.4. UV-Visible DRS Analysis

Pristine TiO_2 and 1, 2.5 and 5% Sr-doped TiO_2 NPs were employed for the analysis of optical properties by UV–visible absorption spectroscopy, as shown in Figure 6a.

Reflectance spectra are presented in Figure 6b. By using the following Kubelka–Munk equation and reflectance data, the optical band gap of the materials was calculated:

$$F(R) = \alpha/s = (1 - R)^2/2R$$

where the terms have their standard and usual meanings. Kubelka–Munk plots of pristine TiO_2 and 1, 2.5 and 5% Sr-doped TiO_2 nanoparticles were drawn using $[F(R\infty)hv]^{1/n}$ Vs eV, and with the help of linear extrapolation of $[F(R\infty)hv]^{1/n}$, their band gaps were determined [63,64]. The estimated band gap values were found to be 3.19, 3.16, 3.18 and 3.20 eV for pristine TiO_2 and 1%, 2.5% and 5% Sr-doped TiO_2 NPs, respectively. The small changes in the band gap could be due to the incorporation of impurities or vacancy defect levels between V.B. and C.B.; this may result in a change in the activity of the materials in terms of their photo- and electrocatalytic applications [46,67].

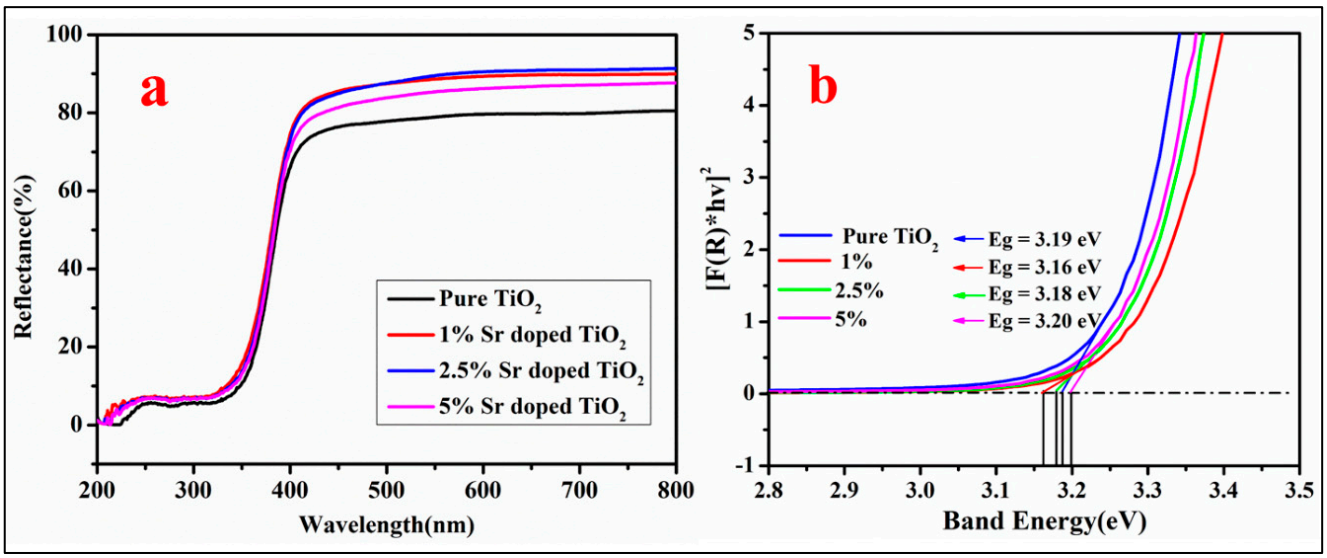

Figure 6. (**a**) UV−vis DRS and (**b**) Kubelka−Munk plots of pristine TiO_2 and 1, 2.5 and 5% Sr-doped TiO_2 NPs.

3.5. Raman Analysis

Raman spectroscopy is a characterization technique used to investigate the structure of complex metal oxides. This technique was used to explore the different vibrational modes of pristine and Sr-doped TiO_2 nanoparticles. For the TiO_2 anatase phase, 15 optical modes were found: $1A_{1g} + 1A_{2u} + 2B_{1g} + 1B_{2u} + 3E_g + 2E_u$ with normal vibrations; six of these are Raman active modes represented by $1A_{1g}$, $2B_{1g}$ and $3E_g$ symmetries. The vibration modes A_{1g}, B_{1g} and E_g arise from antisymmetric, symmetric bending and symmetric stretching of O–Ti–O bending vibrations in the TiO_2 lattice, respectively. As shown in Figure 7, the Raman peaks at 143, 195, 393, 510 and 635 cm^{-1} correspond to the E_g, E_g, B_{1g}, $A_{1g} + B_{1g}$ and Eg modes, respectively [51,68,69]. Comparing the Raman spectrum of pristine and Sr-doped TiO_2, a small blue shift was found due to Sr doping. The principal Raman peak at the E_g (143) mode arises due to external vibration of the anatase structure, which is attributable to the formation of the anatase phase [51,70]. This Raman spectrum was found to be compatible with XRD results.

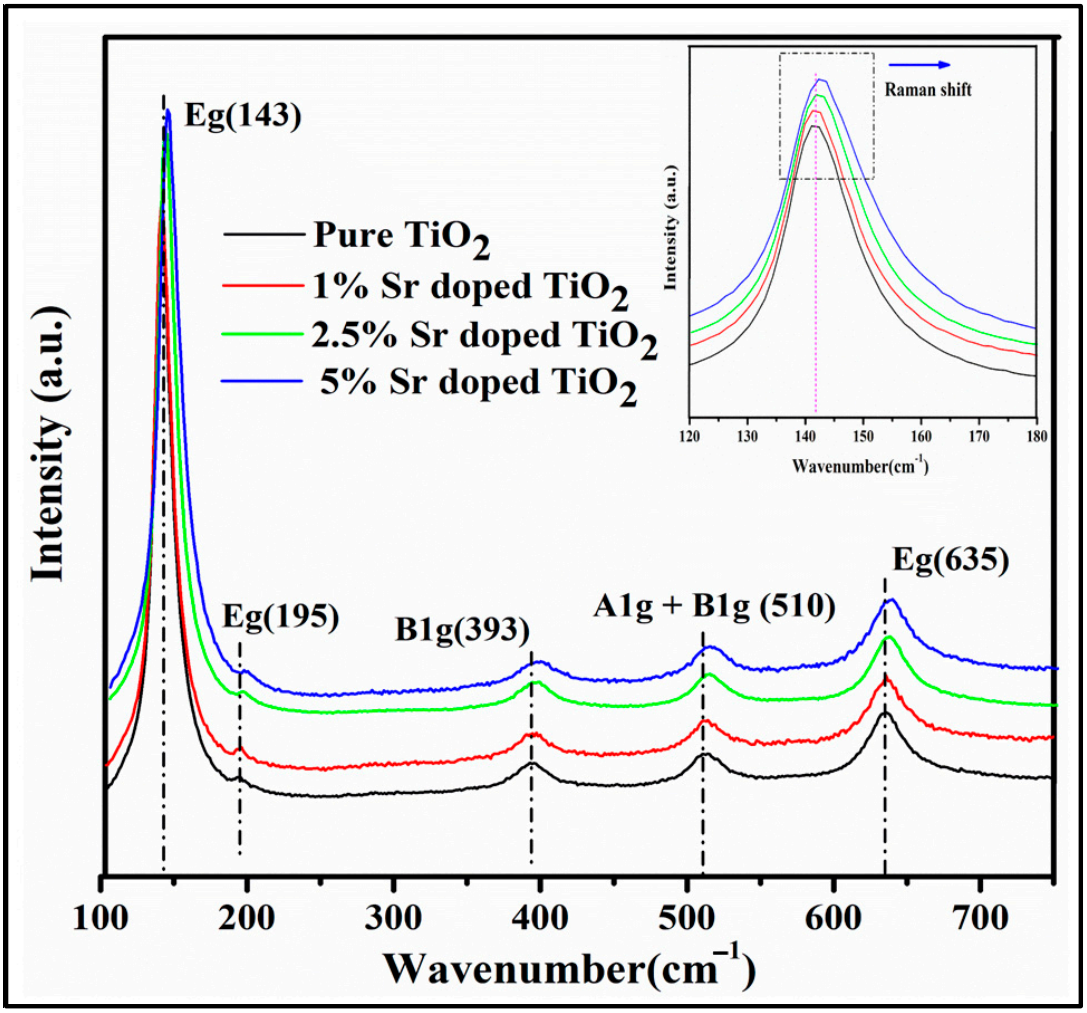

Figure 7. Raman spectra of pristine TiO_2 and Sr-doped TiO_2 nanoparticles.

3.6. BET Surface Area Studies

The catalytic property of materials depends upon the surface area, as the greater surface area of the catalyst is, the greater the number of surface-active sites. Therefore, to examine the catalytic activity of as-prepared nanomaterials, the surface areas of the as-synthesized pristine TiO_2 and 1, 2.5 and 5% Sr-doped TiO_2 nanoparticles were determined. BET results, as shown in Figure 8a for all the as-synthesized samples, have type-IV isotherms and a H3 hysteresis loop. With the help of BET surface area analysis, the specific surface areas of the as-synthesized pristine TiO_2 and 1, 2.5 and 5% Sr-doped TiO_2 nanoparticles were determined and found to be 169, 182, 178 and 141.16 m^2g^{-1}, respectively. The surface area results were associated with the grain size trend, as observed in TEM and SEM studies of Sr-doped TiO_2 NPs. The average pore size distributions calculated by BJH studies of the as-synthesized pristine TiO_2 and 1, 2.5 and 5% Sr-doped TiO_2 nanoparticles were found to be 17.03 ± 0.85, 16.95 ± 0.85, 16.97 ± 0.85 and 16.94 ± 0.85 Å, respectively, as depicted in Figure 8b, which reveals the mesoporous nature of the samples. The pore radius was calculated by using the Dubinin and Astakov (DA) method and was found to be 7–30 Å; the onset of the plots was observed at 14.0, 14.2, 14.0 and 13.7 Å for the pristine TiO_2 and 1, 2.5 and 5% Sr-doped TiO_2 NPs, respectively, as shown in Figure 8c. The surface area investigation with the band gap of as-synthesized materials is presented in Table 1. Further, from the results of UV-DRS and BET surface area, it was observed that the increase in surface area with the decrease in the particle size causes a decrease in the band gap of the nanoparticles, as reported in the literature [53,63,64].

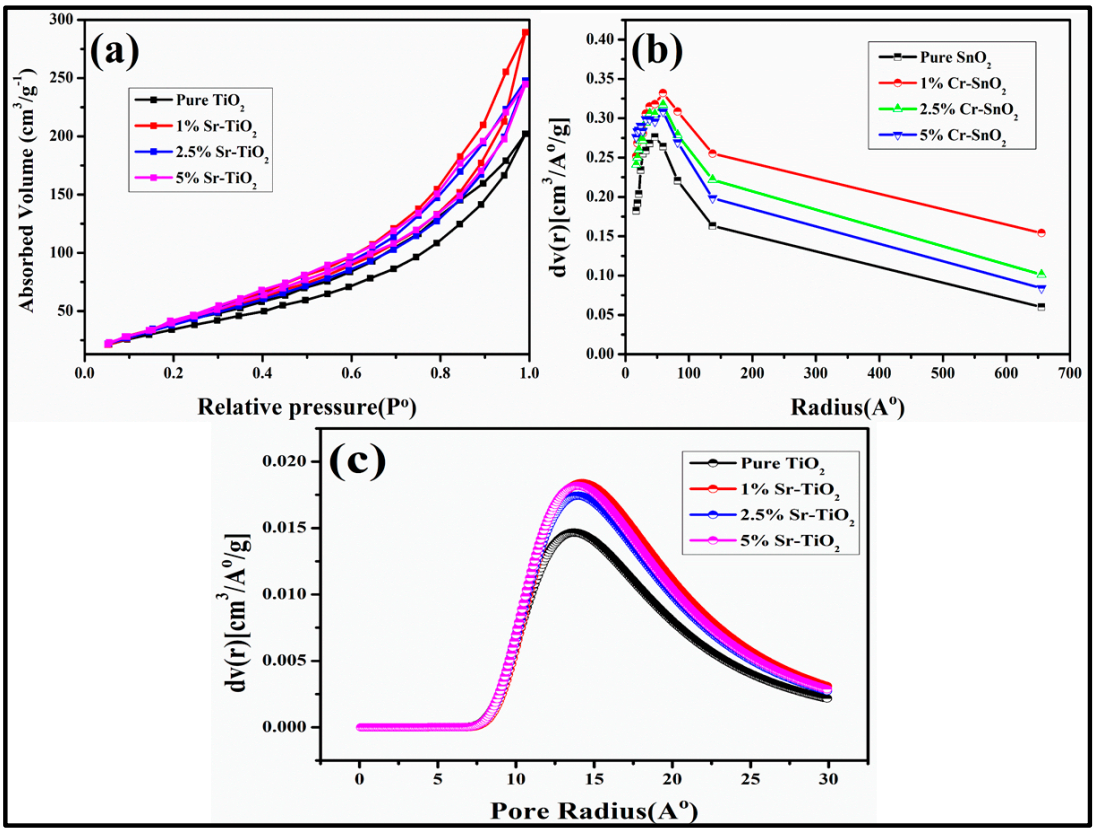

Figure 8. (**a**) Nitrogen adsorption-desorption isotherms, (**b**) BJH pore-size distribution and (**c**) DA average pore-size distribution plots of pristine, 1, 2.5 and 5% Sr-doped TiO_2 NPs.

Table 1. BET surface area (S_{BET}), average pore size, pore volume (V_{total}) and energy band gaps (Eg) of as-synthesized nanocatalysts.

Sample	$S_{BET}/(m^2g^{-1})$	Average Pore Size/Å	$V_{total}/(cm^3g^{-1})$	Eg/eV
Pristine TiO_2	169.9	17.02 ± 0.85	0.359	3.19
1% Sr-doped TiO_2	182.2	16.95± 0.85	0.351	3.16
2.5% Sr-doped TiO_2	178.3	16.97 ± 0.85	0.426	3.18
5% Sr-doped TiO_2	141.2	16.94 ± 0.85	0.294	3.20

3.7. Photocatalytic Water Splitting for Hydrogen Generation

The catalytic activity of as-synthesized nanoparticles was investigated for photocatalytic hydrogen generation by using water-splitting studies. The production of hydrogen is measured as a function of time, as shown in Figure 9a. The total apparent hydrogen evolution after 8 h was found to be 26.3, 16.8, 9.8 and 12.4 $mmolg_{cat}^{-1}$ for 1%, 2.5%, 5% Sr-doped TiO_2 and pristine TiO_2 nanoparticles, respectively, as shown in Figure 9b. The order of photocatalysts on the basis of hydrogen evolution activity is 1% Sr-doped TiO_2 > 2.5% Sr-doped TiO_2 > PristineTiO_2 > 5% Sr-doped TiO_2. Furthermore, 1%, 2.5% and 5% Sr-doped TiO_2 and pristine TiO_2 photocatalysts evolve an average per hour hydrogen of 3.3, 2.1, 1.2 and 1.6 $mmolg_{cat}^{-1}h^{-1}$, respectively, as presented in Figure 9c and comparison of results of the photocatalytic performance of metal-doped TiO_2 synthesized by different methods with present work summarized in Table 2. The photocatalytic activity of 1% Sr-doped TiO_2 was found to be maximum with respect to other compositions and pristine TiO_2 photocatalyst. The increase of the Sr dopant concentration to the host TiO_2 NPs influences the hydrogen evolution rate and decreased the photocatalytic activity after attaining the maximum, as shown in Figure 9b. This study concludes that Sr dopant shows

the corrosive effect of increasing concentration towards hydrogen evolution. A similar trend of corrosiveness was previously reported for Ag-doped SnO_2 nanoparticles [25]. The reproducibility experiment was performed under the same experimental conditions to analyze the stability and repeating ability of the as-synthesized photocatalysts for an 8 h reaction time. Here, the quantitative analysis of hydrogen evolution was performed with a gas chromatography analyzer. The rate of hydrogen evolution, reproducibility and stability were examined for three consecutive cycles, as depicted in Figure 9d. The experimental results show that the first and second cycles have approximately no change in hydrogen evolution (26.30 mmol g_{cat}^{-1}) in 8 h, but in the third cycle, a small decrease in hydrogen evolution (25.93 mmol g_{cat}^{-1}) was observed.

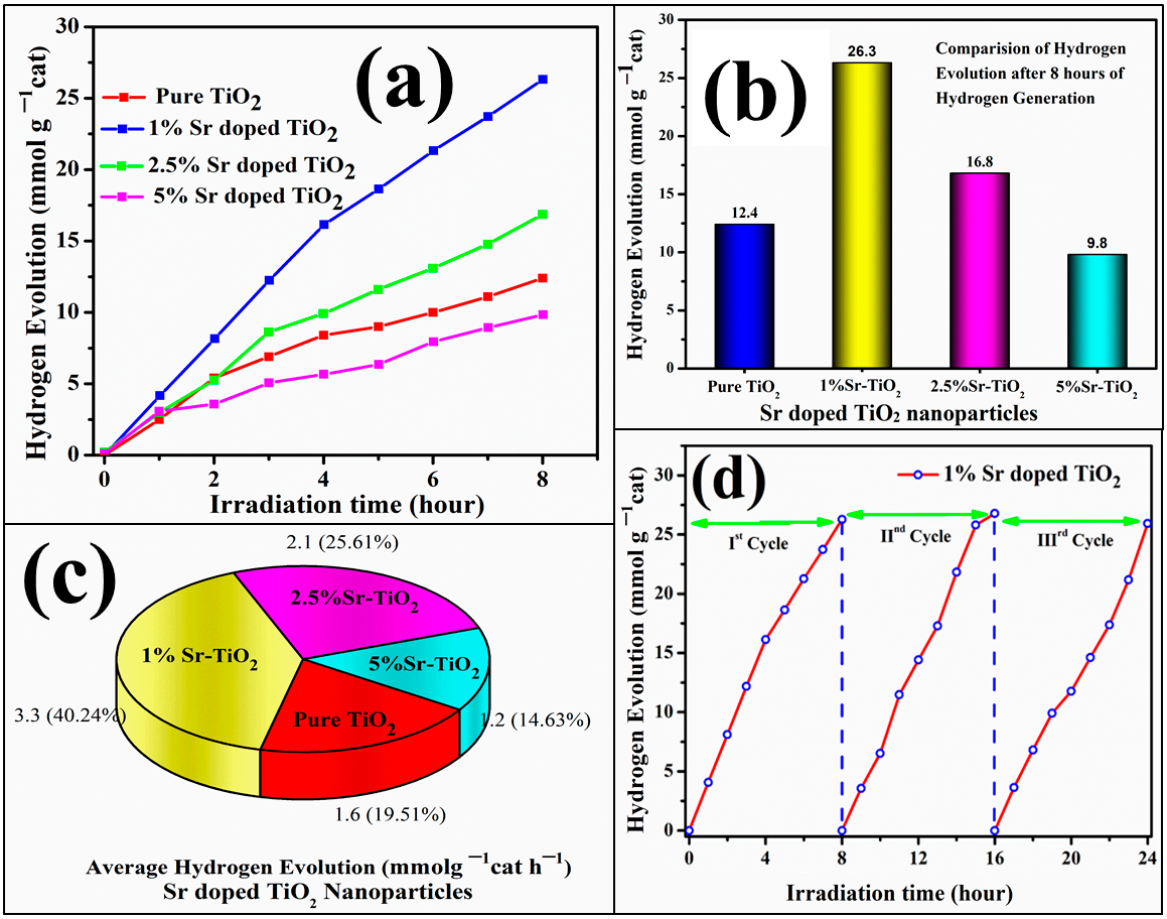

Figure 9. (**a**) Photocatalytic hydrogen evolution curves under UV-visible light irradiation as a function of irradiation time; (**b**) comparison of photocatalytic activity; (**c**) average H_2 evolution per hour of the pristine TiO_2 and 1, 2.5 and 5% Sr-doped TiO_2 NPs; (**d**) stability test of 1% Sr-doped TiO_2 for up to three cycles.

Table 2. Comparison of the photocatalytic performance of metal-doped TiO_2 synthesized by different methods.

S.No.	Dopant	Synthesis Method	Parameters	Hydrogen Production	Ref.
1.	Bismuth, nitrogen	Sol-gel method	Solar light, methanol	1800 µmol/g	[71]
2.	Nitrogen	Solid state/calcination method	UV–Vis light irradiation, Na_2S/Na_2SO_3	18 µmol	[72]
3.	Platinum, nitrogen	Photodeposition method	1150 mL Pyrex vessel, UV light	3200 µmol	[73]
4.	Strontium, silver	Sol–gel method,	500 W Xe arc lamp	49.4 µmol/h	[74]
5.	$Pd/0.2\%K^+$	Hydrothermal method	_	76.6 µmol h−1	[75]
6.	Strontium	Hydrothermal method	200 W, Hg−Xe arc lamp	3.3 $mmol g_{cat}^{-1} h^{-1}$	In this work

3.8. Possible Photocatalytic Reaction Mechanism of Sr-doped TiO_2 Nanoparticles

The hydrogen evolution of pristine TiO_2 and Sr-doped TiO_2 NPs as photocatalysts is illustrated in Figure 10. Here, the photocatalytic efficiency of pristine TiO_2 was observed to be less due to the recombination tendency of photo-induced e^-/h^+. Furthermore, the Sr-doped TiO_2 shows enhanced hydrogen evolution due to a decrease in the recombination tendency by enlarging the band gap and by providing more catalytic active sites, which are generated by enhancing the active surface area [25,63,64]. The photocatalysis efficiency is increased not only by suppressing the e^-/h^+ recombination, but also because of more generation of hydroxyl radicals ($^\bullet$OH). Since Sr-doped TiO_2 NPs involve the replacement of some Sr^{2+} ions by Ti^{4+} ions, which cause charge imbalances, OH^- ions might be adsorbed at the catalyst surface and accept photogenerated holes, generating $^\bullet$OH. This favors the suppuration of photo-induced charge carriers and suppresses the recombination rate. In addition, Sr-doped TiO_2 NPs in solution easily provide electrons to H^+ ions, which facilitates the hydrogen evolution of the system [51,76]. Hence, the holes generated because of electron abstracting by H^+ ions at the valence band of pristine and Sr-doped TiO_2 nanoparticles as photocatalysts were consumed by the sacrificial agents sodium sulphide and sodium sulphite. To summarize, strontium doping causes increased surface area, altering the band gap and inducing defects, which are the reasons for the photocatalytic efficiency of the Sr-doped TiO_2 photocatalysts due to their suppressing the photo-induced e^-/h^+ recombination rate. The possible multi-step reaction for hydrogen evolution based on active sites and adsorbed excited state HS^- species is as follows:

Path A:

$$H_2O + *(\text{active sites}) \rightarrow *OH^- + H^+$$

$$OH^- + h^+ \rightarrow *OH$$

$$2OH \rightarrow H_2O_2 \rightleftharpoons OOH + H^+ \rightleftharpoons O_2^{2-} + 2H^+$$

$$H_2O_2\,(a) + 2h^+ \rightarrow O_2 + 2H^+$$

$$OOH(a) + 2h^+ \rightarrow O_2 + H^+$$

$$O_2^{2-}(a) + 2h^+ \rightarrow O_2$$

$$2H + \rightarrow H_2$$

Path B:

$$HS^-(aq) \rightarrow HS^-(ads) \xrightarrow{hv} [HS^-(ads)]*$$

$$[HS^-(ads)]^* \rightarrow H^* + S^-(ads)$$

$$S^{-}(ads) + [HS^{-}(ads)]* \rightarrow [HS_2^{2-}]\dagger$$

$$[HS_2^{2-}]\dagger \rightarrow H* + S_2^{2-}(ads)$$

$$2H^* \rightarrow H_2$$

$$[HS^{-}(ads)]^* + H_2O \rightarrow S^0\ (ads) + H_2 + OH^{-}$$

Here, ads = adsorption, * = excited state species and † = species undergoing intramolecular charge transfer [1,77,78].

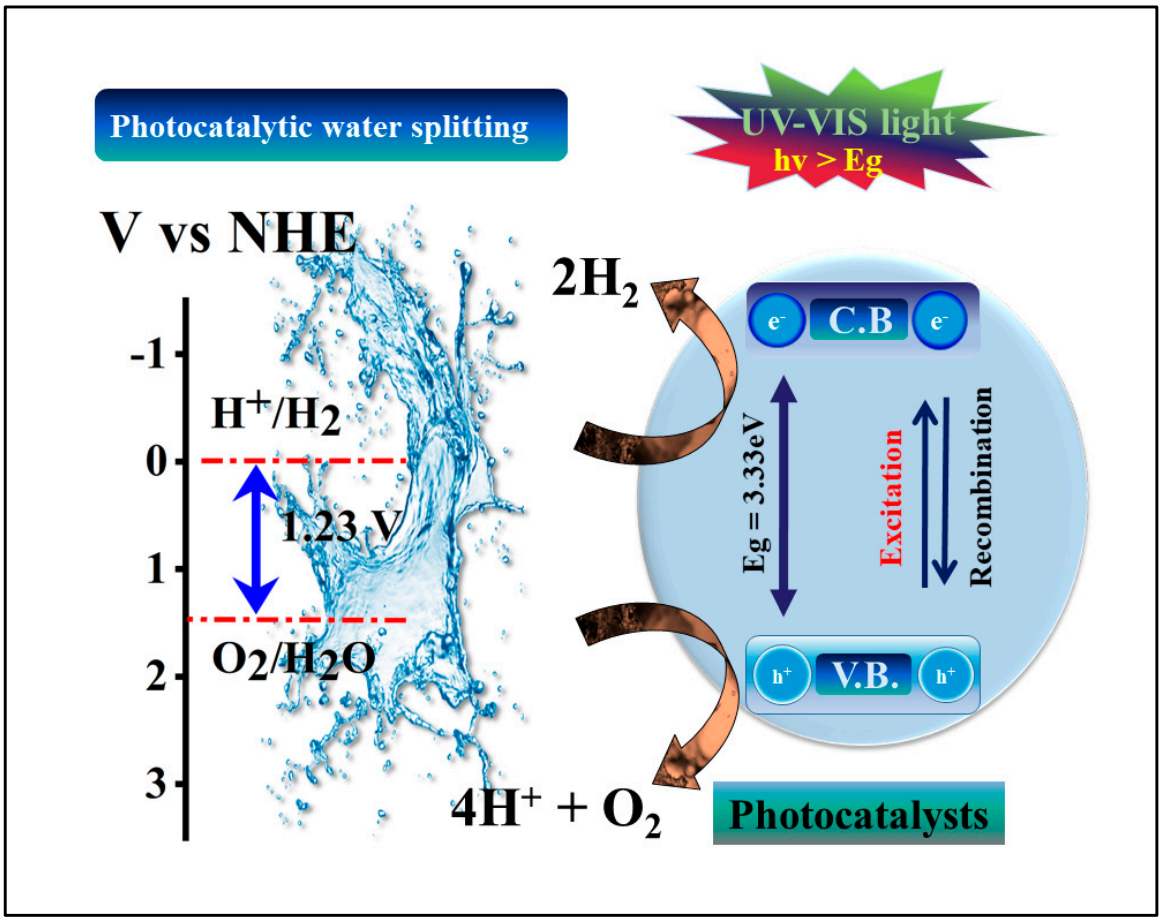

Figure 10. Schematic mechanism of the photocatalytic water splitting for H_2 evolution.

3.9. Electrocatalytic Water Splitting Studies

The electrocatalytic activity of as-synthesized pristine TiO_2 and 1%, 2.5%, 5% Sr-doped TiO_2 NPs as electrocatalysts towards HER (Hydrogen evolution reaction) and OER (Oxygen evolution reaction) performances were determined using a three-electrode configuration in 0.5 N H_2SO_4 and 0.1 N KOH electrolytic solutions under ambient conditions, as demonstrated in Figures 11 and 12. Here, HER responses were investigated by linear sweep voltammetry (LSV) and cyclic voltammetry (CV), as shown in Figure 11a–c. With the increase in the Sr concentration in TiO_2 nanocatalyst, an increase in the overpotential was observed at 10 mA/cm^{-2} cathode current density, which revealed that 1% Sr-doped TiO_2 has high electrocatalytic HER activity. The overpotential values of pristine TiO_2, 1%, 2.5% and 5% Sr-doped TiO_2 electrocatalysts at 10 mA cm^{-2} were 1.00, 0.96, 1.07 and 1.08 V, respectively. The OER performances of pristine TiO_2 and 1%, 2.5% and 5% Sr-doped TiO_2 nanoparticles were evaluated by LSV and CV measurements, as depicted in Figure 13a–c. From the LSV results of OER, superior electrocatalytic activity was shown by 5 % Sr-doped

TiO_2 nanostructures, with an onset potential of 0.8 V as shown in Figure 13a, and an increase in its anodic current density, which produced 2.49 mA/cm^2 at 1.55 V applied potential. Compared with the previously reported current density versus RHE generated by IrO_2, the present works results with 5 % Sr-doped TiO_2 at 1.55 V were ~3.01 and 2.49 mA cm^{-2}, respectively, showing that 5% Sr-doped TiO_2 electrocatalyst has approximately similar potential as IrO_2 electrocatalyst [53,79]. With the help of HER and OER responses, the reaction kinetics and mechanism for electrocatalytic activity were elucidated using Tafel analysis. The reaction kinetics and mechanism are completely correlated with characteristic properties of nanoparticles (such as size, surface area, morphology and optical properties) and orientation of electrocatalysts [4,39,53,80]. Figures 11d and 12d illustrate the Tafel polarization plots of the as-synthesized pristine TiO_2 and 1%, 2.5% and 5% Sr-doped TiO_2 electrocatalysts for the water electrocatalysis. The observed electrodic parameters (HER and OER) are presented in Table 3. The decrease in resistance on the applied potential window were monitored at different scan rates from 10–100 mV. Chronoamperometric (CA) measurements were taken to test the durability and stability of 1% Sr-doped TiO_2 electrocatalyst operating at a voltage of-0.5 V; there was no change found in current density, which was almost stable, as shown in Figure 13. The stability of 5% Sr-doped TiO_2 was also examined through CA at 0.5 V voltage by running for up to 8000 s; it was observed that the current density was stable throughout the measurement (Figure 13). With the help of CV measurement of optimum HER and OER, electrocatalysis of 1% Sr-doped TiO_2 and 5% Sr-doped TiO_2 was carried out, as shown in Figure 11d,e and Figure 12c, respectively.

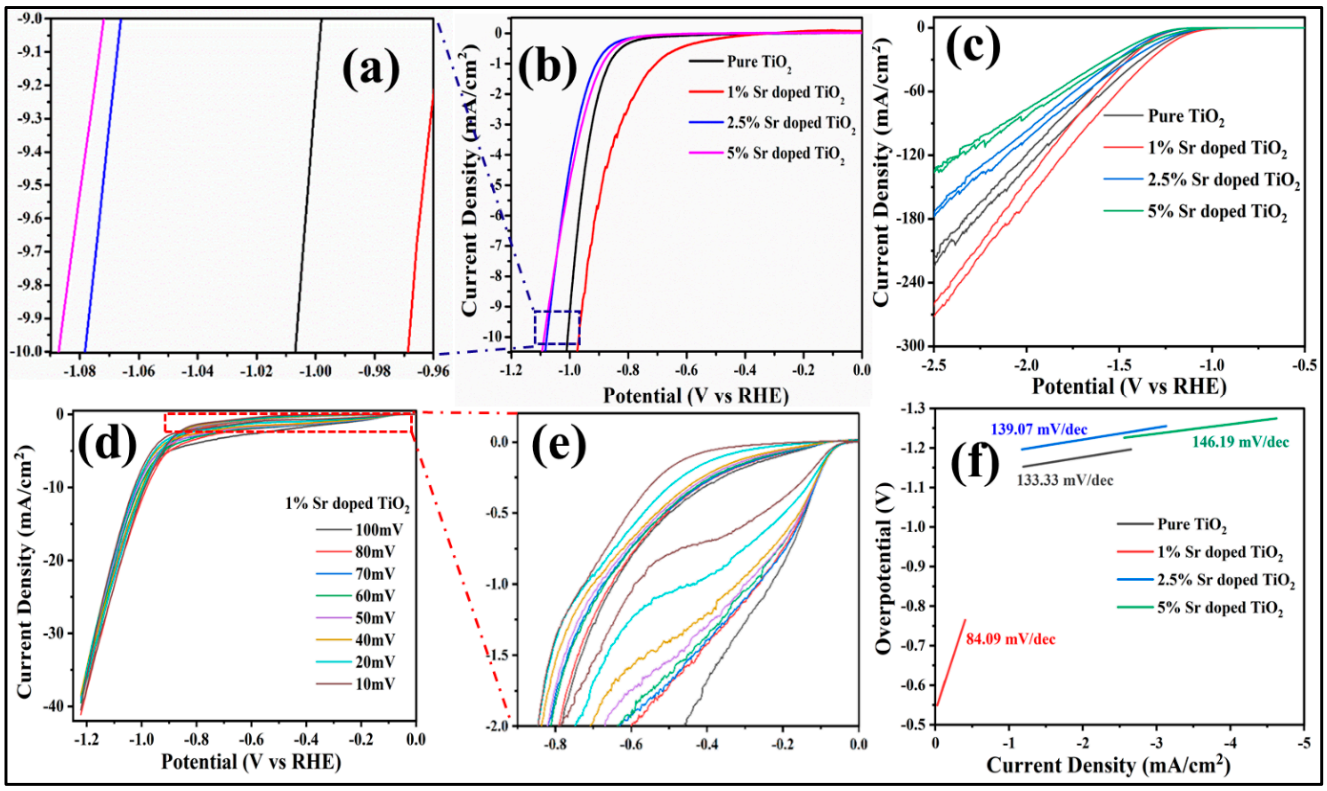

Figure 11. (**a**–**c**) shows the LSV and CV plots of HER of as-synthesized pristine TiO_2 and 1%, 2.5% and 5% Sr-doped TiO_2; (**d**,**e**) shows the CV plots of 1% Sr-doped TiO_2 toward HER; (**f**) shows HER Tafel plots of pristine TiO_2 and 1%, 2.5% and 5% Sr-doped TiO_2.

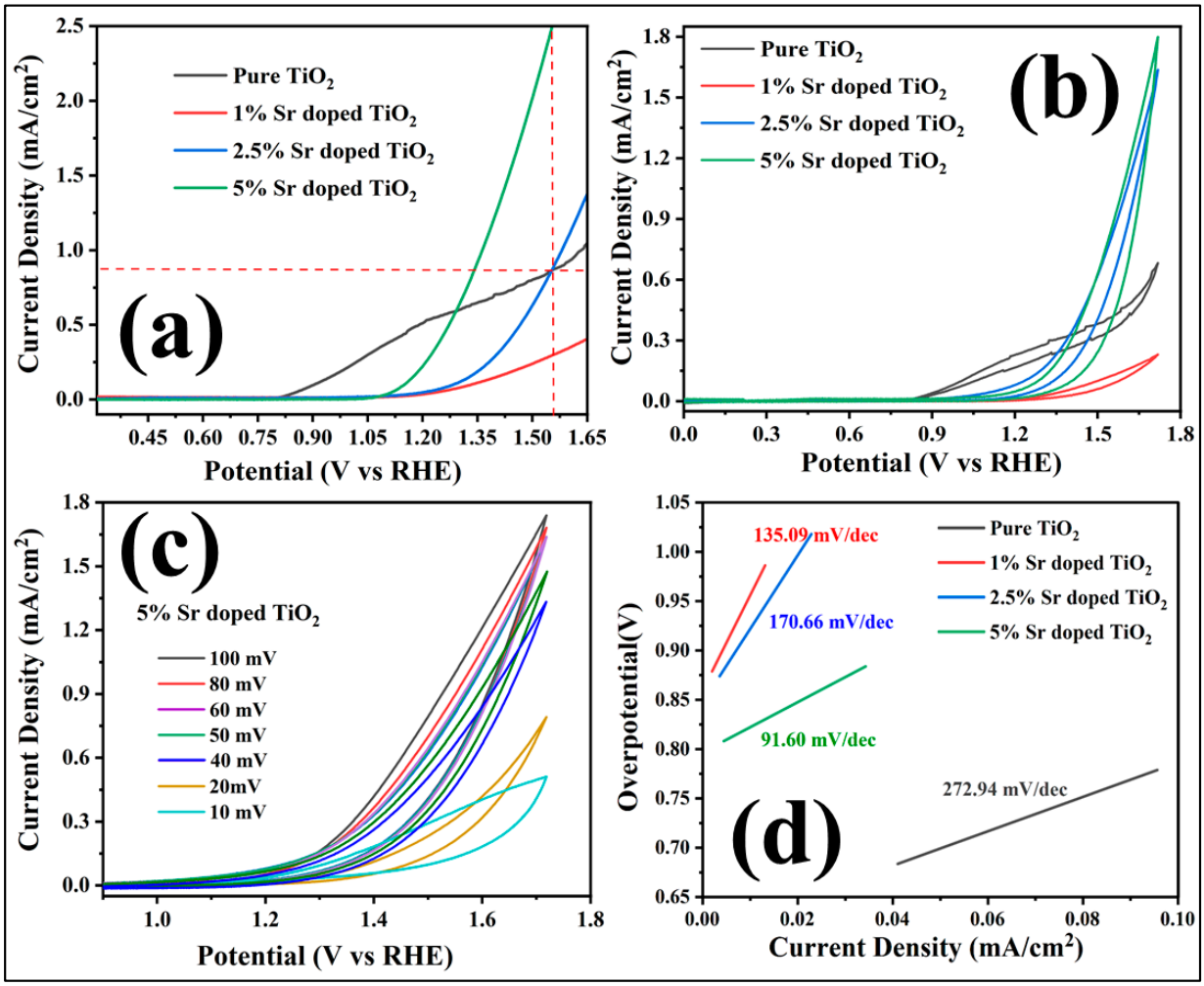

Figure 12. (**a**,**b**) shows the LSV and CV plots of OER of as-synthesized pristine TiO_2 and 1%, 2.5% and 5% Sr-doped TiO_2; (**c**) shows the CV plots of 5% Sr-doped TiO_2 toward OER; (**d**) shows the OER Tafel plots of as-synthesized pristine TiO_2 and 1%, 2.5% and 5% Sr-doped TiO_2.

Table 3. HER and OER electrodic parameters of pristine and Sr-doped TiO_2 electrocatalysts.

S.No	Materials	HER		OER		
		Overpotential (V) to Attain 10 mA/cm^2	Tafel Slope (mV/dec)	Onset Potential (V)	Anodic Current Density (mA/cm^2) at 1.55 V	Tafel Slope (mV/dec)
1.	Pristine TiO_2	1.00	133.33	0.8	0.86	272.94
2.	1% Sr-doped TiO_2	0.96	84.09	1.23	0.30	135.09
3.	2.5% Sr-doped TiO_2	1.07	139.07	1.34	0.87	170.66
4.	5% Sr-doped TiO_2	1.08	146.16	1.1	2.49	91.60

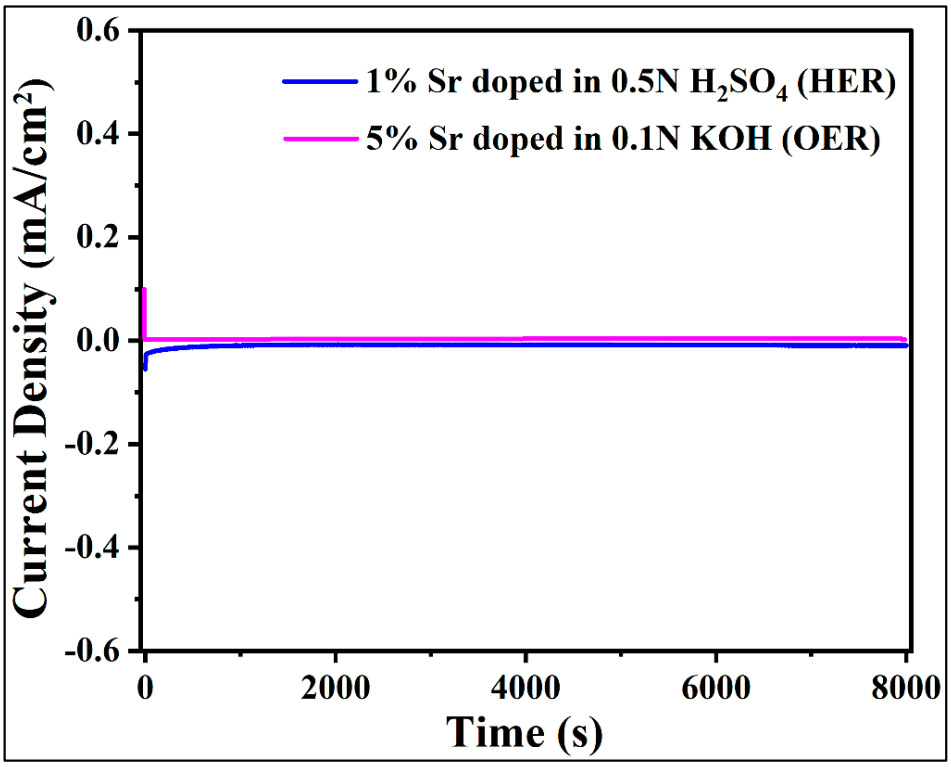

Figure 13. CA analysis at −0.5 V and +0.5 V for 1% and 5% Sr-doped TiO_2 nanoparticles.

4. Conclusions

Pristine anatase TiO_2 and Sr-doped TiO_2 nanocatalysts with highly crystalline and tetragonal structure were successfully synthesized with an eco-friendly low-temperature hydrothermal method. Due to the various reinforcing and synergistic factors of the cubical architectures of the TiO_2 and its dopants, such as increased surface area, the introduction of defects created by doping and the band gap tuning of the material resulted in an enhanced photocatalytic and electrocatalytic performance. One-percent Sr-doped TiO_2 showed the best photocatalytic and electrocatalytic HER activity and 5% Sr-doped TiO_2 displayed optimum electrocatalytic activity towards OER. The maximum H_2 production of 1% Sr-doped TiO_2 was found to be 26.3 mmolg_{cat}^{-1}. Furthermore, 1% and 5% Sr-doped TiO_2 electrocatalysts showed maximum current density for both HER (≈10 mA/cm^2) and OER (≈2.49 mA/cm^2), with an onset potential of 0.96 V for HER and 1.55 V for OER with Tafel slopes of 84.09 and 91.60 mV/dec, respectively. The increase in the photocatalytic and electrocatalytic performances of the photo/electrocatalysts was attributed to the high specific surface areas and the tuning of the band gap introduced by the incorporation of dopants, and resulted in an overall increase in performance. The study thus reveals that the synthesized compounds can act as efficient materials for photo/electrocatalysis for water-splitting hydrogen evolution and current density for HER and OER, which makes them potential candidates for green/renewable energy resources.

Author Contributions: M.F. is responsible experimental investigation, data collection, measurements, analysis and rough draft of the manuscript, whereas T.A. is responsible for analysis, conceptualization, supervision and final draft of the manuscript. All authors have read and agreed to the published version of the manuscript.

Funding: TA thanks UGC, New Delhi, Govt. of India for the Research Grant for In-service Faculty Members. The authors also thank SERB, CSIR and MoE (SPARC/2018-2019/P843/SL) for financial support to Nano Chemistry and Nano Energy Labs.

Institutional Review Board Statement: Not applicable.

Informed Consent Statement: Not applicable.

Data Availability Statement: Not applicable.

Acknowledgments: TA thanks UGC, New Delhi, Govt. of India for the Research Grant for In-service Faculty Members. The authors also thank SERB, CSIR and MoE (SPARC/2018-2019/P843/SL) for financial support to Nano Chemistry and Nano Energy Labs. MF thanks to UGC, New Delhi for the research fellowship. The authors also acknowledge the measurement support provided through the DST PURSE program at CIF, JMI and AIIMS, New Delhi for electron microscopic studies.

Conflicts of Interest: The authors declare no financial competing interest.

References

1. Kumaravel, V.; Mathew, S.; Bartlett, J.; Pillai, S.C. Photocatalytic hydrogen production using metal doped TiO_2: A review of recent advances. *Appl. Catal. B Environ.* **2019**, *244*, 1021–1064. [CrossRef]
2. Mehtab, A.; Banerjee, S.; Mao, Y.; Ahmad, T. Type-II $CuFe_2O_4$/Graphitic Carbon Nitride Heterojunctions for High-Efficiency Photocatalytic and Electrocatalytic Hydrogen Generation. *ACS Appl. Mater. Interfaces.* **2022**, *14*, 44317–44329. [CrossRef] [PubMed]
3. Gautam, A.; Sk, S.; Pal, U. Recent Advances in Solution Assisted Synthesis of Transition Metal Chalcogenides for Photo-electro Catalytic Hydrogen Evolution. *Phys. Chem.* **2022**, *24*, 20638–20673.
4. Mehtab, A.; Alshehri, S.M.; Ahmad, T. Photocatalytic and Photoelectrocatalytic Water Splitting by Porous g-C_3N_4 Nanosheets for Hydrogen Generation. *ACS Appl. Nano Mater.* **2022**, *5*, 12656–12665. [CrossRef]
5. Ali, S.A.; Ahmad, T. Chemical strategies in molybdenum based chalcogenides nanostructures for photocatalysis. *Int. J. Hydrog. Energy* **2022**, *29*, 29255–29283. [CrossRef]
6. Xu, X.; Song, F.; Hu, X. A nickel iron diselenide-derived efficient oxygen-evolution catalyst. *Nat. Commun.* **2016**, *7*, 1–7. [CrossRef] [PubMed]
7. Pandit, N.A.; Ahmad, T. Tin Oxide Based Hybrid Nanostructures for Efficient Gas Sensing. *Molecules* **2022**, *27*, 7038–7082. [CrossRef]
8. Mehtab, A.; Ahmed, J.; Alshehri, S.M.; Mao, Y.; Ahmad, T. Rare earth doped metal oxide nanoparticles for photocatalysis: A perspective. *Nanotechnology* **2022**, *33*, 142001. [CrossRef]
9. Joy, J.; Mathew, J.; George, S.C. Nanomaterials for photoelectrochemical water splitting-review. *Int. J. Hydrog. Energy* **2018**, *43*, 4804–4817. [CrossRef]
10. Naaz, F.; Sharma, A.; Shahazad, M.; Ahmad, T. Hydrothermally Derived Hierarchical CuO Nanoflowers as an Efficient Photocatalyst and Electrocatalyst for Hydrogen Evolution. *ChemistrySelect* **2022**, *7*, e202201800. [CrossRef]
11. Farooq, U.; Ahmed, J.; Alshehri, S.M.; Mao, Y.; Ahmad, T. Self-Assembled Interwoven Nanohierarchitectures of $NaNbO_3$ and $NaNb_{1-x}Ta_xO_3$ ($0.05 \leq x \leq 0.20$): Synthesis, Structural Characterization, Photocatalytic Applications, and Dielectric Properties. *ACS Omega* **2022**, *7*, 16952–16967. [CrossRef] [PubMed]
12. Basavarajappa, P.S.; Patil, S.B.; Ganganagappa, N.; Reddy, K.R.; Raghu, A.V.; Reddy, C.V. Recent progress in metal-doped TiO_2, non-metal doped/codoped TiO_2 and TiO_2 nanostructured hybrids for enhanced photocatalysis. *Int. J. Hydrog. Energy* **2020**, *45*, 7764–7778. [CrossRef]
13. Samuel, E.; Joshi, B.; Kim, M.; Swihart, M.T.; Yoon, S.S. Morphology engineering of photoelectrodes for efficient photoelectrochemical water splitting. *Nano Energy* **2020**, *72*, 104648. [CrossRef]
14. Liu, Q.; Shi, J.; Xu, Z.; Zhang, B.; Liu, H.; Lin, Y.; Gao, F.; Li, S.; Li, G. InGaN Nanorods Decorated with Au Nanoparticles for Enhanced Water Splitting Based on Surface Plasmon Resonance Effects. *Nanomaterials* **2020**, *10*, 912. [CrossRef] [PubMed]
15. Xu, Z.; Zhang, S.; Liang, J.; Lin, J.; Yu, Y.; Li, R.; Gao, F.; Li, G. Surface passivation of InGaN nanorods using H_3PO_4 treatment for enhanced photoelectrochemical performance. *J. Power Sources* **2019**, *419*, 65–71. [CrossRef]
16. Zhang, N.; Liu, S.; Fu, X.; Xu, Y. Synthesis of M@TiO_2 (M= Au, Pd, Pt) core–shell nanocomposites with tunable photoreactivity. *J. Phys. Chem. C* **2011**, *115*, 9136–9145. [CrossRef]
17. Idriss, H. The elusive photocatalytic water splitting reaction using sunlight on suspended nanoparticles: Is there a way forward? *Catal. Sci. Technol.* **2020**, *10*, 304–310. [CrossRef]
18. Zhang, H.; Liang, C.; Liu, J.; Tian, Z.; Wang, G.; Cai, W. Defect-mediated formation of Ag cluster-doped TiO_2 nanoparticles for efficient photodegradation of pentachlorophenol. *Langmuir* **2012**, *28*, 3938–3944. [CrossRef]
19. Wang, W.; Jin, C.; Qi, L. Hierarchical CdS nanorod@SnO_2 nanobowl arrays for efficient and stable photoelectrochemical hydrogen generation. *Small* **2018**, *14*, 1801352. [CrossRef]
20. Guo, C.X.; Xie, J.; Yang, H.; Li, C.M. Au@CdS Core–Shell Nanoparticles-Modified ZnO Nanowires Photoanode for Efficient Photoelectrochemical Water Splitting. *Adv. Sci. Lett.* **2015**, *2*, 1500135. [CrossRef]
21. Cao, S.; Yin, Z.; Barber, J.; Boey, F.Y.; Loo, S.C.J.; Xue, C. Preparation of Au-$BiVO_4$ heterogeneous nanostructures as highly efficient visible-light photocatalysts. *ACS Appl. Mater. Interfaces* **2012**, *4*, 418–423. [CrossRef]
22. Valero, J.M.; Obregón, S.; Colón, G. Active site considerations on the photocatalytic H_2 evolution performance of Cu-doped TiO_2 obtained by different doping methods. *ACS Catal.* **2014**, *4*, 3320–3329. [CrossRef]

23. Yang, J.; Wang, X.; Dai, J.; Li, J. Efficient visible-light-driven photocatalytic degradation with Bi_2O_3 coupling silica doped TiO_2. *Ind. Eng. Chem. Res.* **2014**, *53*, 12575–12586. [CrossRef]
24. Khan, H.; Lone, I.H.; Lofland, S.E.; Ramanujachary, K.V.; Ahmad, T. Exploiting Multiferroicity of $TbFeO_3$ Nanoparticles for Hydrogen Generation through Photo/Electro/Photoelectro-catalytic Water Splitting. *Int. J. Hydrog. Energy* **2022**, *in press*. [CrossRef]
25. Jain, S.K.; Fazil, M.; Naaz, F.; Pandit, N.A.; Ahmed, J.; Alshehri, S.M.; Mao, Y.; Ahmad, T. Silver-doped SnO_2 nanostructures for photocatalytic water splitting and catalytic nitrophenol reduction. *New J. Chem.* **2022**, *46*, 2846–2857. [CrossRef]
26. Wu, M.; Wu, P.; Lin, T.; Lin, T. Photocatalytic performance of Cu-doped TiO_2 nanofibers treated by the hydrothermal synthesis and air-thermal treatment. *Appl. Surf. Sci.* **2018**, *430*, 390–398. [CrossRef]
27. Sulaiman, S.N.A.; Noh, M.Z.; Adnan, N.N.; Bidin, N.; Razak, S.N.A. Effects of photocatalytic activity of metal and non-metal doped TiO_2 for hydrogen production enhancement-a review. *J. Phys. Conf. Ser.* **2018**, *1027*, 012006. [CrossRef]
28. Ko, S.; Banerjee, C.K.; Sankar, J. Photochemical synthesis and photocatalytic activity in simulated solar light of nanosized Ag doped TiO_2 nanoparticle composite. *Compos. B. Eng.* **2011**, *42*, 579–583. [CrossRef]
29. Emran, K.M. Catalytic Activity of Strontium Modified TiO_2 Nanotubes for Hydrogen Evolution Reaction. *Int. J. Electrochem. Sci.* **2020**, *15*, 4218–4231. [CrossRef]
30. Fujishima, A.; Honda, K. Electrochemical photolysis of water at a semiconductor electrode. *Nature* **1972**, *238*, 37–38. [CrossRef]
31. Karunakaran, C.; Abiramasundari, G.; Gomathisankar, P.; Manikandan, G.; Anandi, V. Cu-doped TiO_2 nanoparticles for photocatalytic disinfection of bacteria under visible light. *J. Colloid Interface Sci.* **2010**, *352*, 68–74. [CrossRef] [PubMed]
32. Rohilla, S. Rietveld refinement and structural characterization of $TiO_2/CoFe_2O_4$ nanocomposites. *In IOP Conference Series: Mater. Sci. Eng.* **2020**, *872*, 012171.
33. Yadav, H.M.; Otari, S.V.; Koli, V.B.; Mali, S.S.; Hong, C.K.; Pawar, S.H.; Delekar, S.D. Preparation and characterization of copper-doped anatase TiO_2 nanoparticles with visible light photocatalytic antibacterial activity. *J. Photochem. Photobiol. A* **2014**, *280*, 32–38. [CrossRef]
34. Gogoi, D.; Namdeo, A.; Golder, A.K.; Peela, N.R. Ag-doped TiO_2 photocatalysts with effective charge transfer for highly efficient hydrogen production through water splitting. *Int. J. Hydrog. Energy* **2020**, *45*, 2729–2744. [CrossRef]
35. Tsebriienko, T.; Popov, A.I. Effect of poly (titanium oxide) on the viscoelastic and thermophysical properties of interpenetrating polymer networks. *Crystals* **2021**, *11*, 794. [CrossRef]
36. Jang, D.M.; Kwak, I.H.; Kwon, E.L.; Jung, C.S.; Im, H.S.; Park, K.; Park, J. Transition-metal doping of oxide nanocrystals for enhanced catalytic oxygen evolution. *J. Phys. Chem. C* **2015**, *119*, 1921–1927. [CrossRef]
37. Alshehri, S.M.; Ahmed, J.; Ahamad, T.; Alhokbany, N.; Arunachalam, P.; Al-Mayouf, A.M.; Ahmad, T. Synthesis, characterization, multifunctional electrochemical (OGR/ORR/SCs) and photodegradable activities of $ZnWO_4$ nanobricks. *J. Solgel Sci. Technol.* **2018**, *87*, 137–146. [CrossRef]
38. Behnajady, M.A.; Alizade, B.; Modirshahla, N. Synthesis of Mg-doped TiO_2 nanoparticles under different conditions and its photocatalytic activity. *Photochem. Photobiol.* **2011**, *87*, 1308–1314. [CrossRef]
39. Farooq, U.; Ahmed, J.; Alshehri, S.M.; Ahmad, T. High-surface-area sodium tantalate nanoparticles with enhanced photocatalytic and electrical properties prepared through polymeric citrate precursor route. *ACS Omega* **2019**, *4*, 19408–19419. [CrossRef]
40. Kumar, A.; Patel, A.S.; Mohanty, T. Correlation of photodegradation efficiency with surface potential of silver-TiO_2 nanocomposite thin films. *J. Phys. Chem. C* **2012**, *116*, 20404–20408. [CrossRef]
41. Jung, H.; Yeo, I.; Kim, T.; Ki, H.; Gu, H. Surface plasmon resonance effect of silver nanoparticles on a TiO_2 electrode for dye-sensitized solar cells. *Appl. Surf. Sci.* **2018**, *432*, 266–271. [CrossRef]
42. Barad, H.; Ginsburg, A.; Cohen, H.; Rietwyk, K.J.; Keller, D.A.; Tirosh, S.; Bouhadana, Y.; Anderson, A.Y.; Zaban, A. Hot Electron-Based Solid State TiO_2 | Ag Solar Cells. *Adv. Mater. Interfaces* **2016**, *3*, 1500789. [CrossRef]
43. Zhang, X.; Li, L.; Zhou, Q.; Liang, X.; Liu, D. Facile synthesis of novel gully-like double-sized mesoporous structural Sr-doped ZrO_2-TiO_2 composites with improved photocatalytic efficiency. *J. Solid State Chem.* **2019**, *269*, 375–385. [CrossRef]
44. Hamad, H.; Elsenety, M.M.; Sadik, W.; El-Demerdash, A.; Nashed, A.; Mostafa, A.; Elyamny, S. The superior photocatalytic performance and DFT insights of S-scheme CuO@TiO_2 heterojunction composites for simultaneous degradation of organics. *Sci. Rep.* **2022**, *12*, 1–20. [CrossRef] [PubMed]
45. Nayak, S.; Sahoo, B.; Khastgir, D. Flexible Nanocomposites Comprised of Poly (dimethylsiloxane) and High-Permittivity TiO_2 Nanoparticles Doped with La^{3+}/Cu^{+} for Dielectric Applications. *ACS Appl. Nano Mater.* **2019**, *2*, 4211–4221. [CrossRef]
46. Farooq, U.; Chaudhary, P.; Ingole, P.P.; Kalam, A.; Ahmad, T. Development of cuboidal $KNbO_3$@α-Fe_2O_3 hybrid nanostructures for improved photocatalytic and photoelectrocatalytic applications. *ACS Omega* **2020**, *5*, 20491–20505. [CrossRef]
47. Baruah, M.; Ezung, S.L.; Sharma, S.; Sinha, U.B.; Sinha, D. Synthesis and characterization of Ni-doped TiO_2 activated carbon nanocomposite for the photocatalytic degradation of Anthracene. *Inorg. Chem. Commun.* **2022**, *144*, 109905. [CrossRef]
48. Peng, B.; Meng, X.; Tang, F.; Ren, X.; Chen, D.; Ren, J. General synthesis and optical properties of monodisperse multifunctional metal-ion-doped TiO_2 hollow particles. *J. Phys. Chem. C* **2009**, *113*, 20240–20245. [CrossRef]
49. Hamedani, H.A.; Allam, N.K.; Garmestani, H.; El-Sayed, M.A. Electrochemical fabrication of strontium-doped TiO_2 nanotube array electrodes and investigation of their photoelectrochemical properties. *J. Phys. Chem. C* **2011**, *115*, 13480–13486. [CrossRef]
50. Gobal, F.; Faraji, M. Fabrication of nanoporous nickel oxide by de-zincification of Zn–Ni/(TiO_2-nanotubes) for use in electrochemical supercapacitors. *Electrochim. Acta* **2013**, *100*, 133–139. [CrossRef]

51. Wei, X.; Cao, J.; Fang, F. A novel multifunctional Ag and Sr^{2+} co-doped TiO_2@ rGO ternary nanocomposite with enhanced p-nitrophenol degradation, and bactericidal and hydrogen evolution activity. *RSC Adv.* **2018**, *8*, 31822–31829. [CrossRef]
52. Nguyen, D.C.; Doan, T.L.L.; Prabhakaran, S.; Tran, D.T.; Kim, D.H.; Lee, J.H.; Kim, N.H. Hierarchical Co and Nb dual-doped MoS_2 nanosheets shelled micro-TiO_2 hollow spheres as effective multifunctional electrocatalysts for HER, OER, and ORR. *Nano Energy* **2021**, *82*, 105750. [CrossRef]
53. Farooq, U.; Phul, R.; Alshehri, S.M.; Ahmed, J.; Ahmad, T. Electrocatalytic and enhanced photocatalytic applications of sodium niobate nanoparticles developed by citrate precursor route. *Sci. Rep.* **2019**, *9*, 1–17. [CrossRef] [PubMed]
54. Takahiro, N.; Shinagawa, T.; Nishimoto, T.; Takanabe, K. Recent advances in understanding oxygen evolution reaction mechanisms over iridium oxide. *Inorg. Chem. Front.* **2021**, *8*, 2900–2917.
55. Ahmed, J.; Ahamad, T.; Alhokbany, N.; Almaswari, B.M.; Ahmad, T.; Hussain, A.; Al-Farraj, E.S.S.; Alshehri, S.M. Molten salts derived copper tungstate nanoparticles as bifunctional electro-catalysts for electrolysis of water and supercapacitor applications. *ChemElectroChem* **2018**, *5*, 3938–3945. [CrossRef]
56. Haase, F.T.; Rabe, A.; Schmidt, F.P.; Herzog, A.; Jeon, H.S.; Frandsen, W.; Narangoda, P.V.; Spanos, I.; Friedel Ortega, K.; Timoshenko, J.; et al. Role of Nanoscale Inhomogeneities in Co_2FeO_4 Catalysts during the Oxygen Evolution Reaction. *J. Am. Chem. Soc.* **2022**, *144*, 12007–12019. [CrossRef]
57. Grimes, C.A.; Varghese, O.K.; Ranjan, S. Photoelectrolysis. In *Light, Water, Hydrogen*; Springer: Berlin/Heidelberg, Germany, 2008; pp. 115–190.
58. Zhu, C.; Li, C.; Zheng, M.; Delaunay, J. Plasma-induced oxygen vacancies in ultrathin hematite nanoflakes promoting photoelectrochemical water oxidation. *ACS Appl. Mater. Interfaces* **2015**, *7*, 22355–22363. [CrossRef] [PubMed]
59. Ma, Z.; Zhang, Y.; Liu, S.; Xu, W.; Wu, L.; Hsieh, Y.; Liu, P.; Zhu, Y.; Sasaki, K.; Renner, J.N.; et al. Reaction mechanism for oxygen evolution on RuO_2, IrO_2, and RuO_2@ IrO_2 core-shell nanocatalysts. *J. Electroanal. Chem.* **2018**, *819*, 296–305. [CrossRef]
60. Ahmed, J.; Ubaidullah, M.; Ahmad, T.; Alhokbany, N.; Alshehri, S.M. Synthesis of graphite oxide/cobalt molybdenum oxide hybrid nanosheets for enhanced electrochemical performance in supercapacitors and the oxygen evolution reaction. *ChemElectroChem* **2019**, *6*, 2524–2530. [CrossRef]
61. Ahmad, T.; Ganguli, A.K. Synthesis of nanometer-sized particles of barium orthotitanate prepared through a modified reverse micellar route: Structural characterization, phase stability and dielectric properties. *J. Mater. Res.* **2004**, *19*, 2905–2912. [CrossRef]
62. Ahmad, T.; Ganguli, A.K. Reverse micellar route to nanocrystalline titanates ($SrTiO_3$, Sr_2TiO_4, and $PbTiO_3$): Structural aspects and dielectric properties. *J. Am. Ceram. Soc.* **2006**, *89*, 1326–1332. [CrossRef]
63. Jain, S.; Pandit, N.A.; Fazil, M.; Ali, S.A.; Ahmed, J.; Alshehri, S.M.; Mao, Y.; Ahmad, T. Chemical Fabrication, Structural Characterization and Photocatalytic Water Splitting Application of Sr-Doped SnO_2 Nanoparticles. *Nanotechnology* **2022**, *33*, 355706. [CrossRef] [PubMed]
64. Jain, S.K.; Fazil, M.; Pandit, N.A.; Ali, S.A.; Naaz, F.; Khan, H.; Mehtab, A.; Ahmed, J.; Ahmad, T. Modified, Solvothermally Derived Cr-doped SnO_2 Nanostructures for Enhanced Photocatalytic and Electrochemical Water-Splitting Applications. *ACS Omega* **2022**, *7*, 14138–14147. [CrossRef] [PubMed]
65. Fan, X.; Hua, N.; Jia, H.; Zhu, Y.; Wang, Z.; Xu, J.; Wang, C. Synthesis and evaluation of visible-light photocatalyst: Nitrogen-doped TiO_2/Bi_2O_3 heterojunction structures. *Sci. Adv. Mater.* **2014**, *6*, 1892–1899. [CrossRef]
66. Mohamed, I.M.; Dao, V.; Yasin, A.S.; Barakat, N.A.; Choi, H. Design of an efficient photoanode for dye-sensitized solar cells using electrospun one-dimensional GO/N-doped nanocomposite SnO_2/TiO_2. *Appl. Surf. Sci.* **2017**, *400*, 355–364. [CrossRef]
67. Brik, M.G.; Srivastava, A.M.; Popov, A.I. A few common misconceptions in the interpretation of experimental spectroscopic data. *Opt. Mater.* **2022**, *127*, 112276. [CrossRef]
68. Saqib, M.; Althubeiti, K.; Abualnaja, K.M.; Rahman, N.; Khan, R. Effect of Sr and Co co-doping on the TiO_2-diluted magnetic semiconductor for spintronic applications. *J. Mater. Sci.: Mater. Electron.* **2021**, *32*, 28718–28729.
69. Ekoi, E.J.; Gowen, A.; Dorrepaal, R.; Dowling, D.P. Characterisation of titanium oxide layers using Raman spectroscopy and optical profilometry: Influence of oxide properties. *Results Phys.* **2019**, *12*, 1574–1585. [CrossRef]
70. Yang, G.; Jiang, Z.; Shi, H.; Xiao, T.; Yan, Z. Preparation of highly visible-light active N-doped TiO_2 photocatalyst. *J. Mater. Chem.* **2010**, *20*, 5301–5309. [CrossRef]
71. Kumar, M.K.; Bhavani, K.; Srinivas, B.; Kumar, S.N.; Sudhakar, M.; Naresh, G.; Venugopal, A. Nano structured bismuth and nitrogen co-doped TiO_2 as an efficient light harvesting photocatalyst under natural sunlight for the production of H_2 by H_2O splitting. *Appl. Catal. A* **2016**, *515*, 91–100. [CrossRef]
72. Zhang, X.; Song, P.; Cui, X. Nitrogen-doped TiO_2 photocatalysts synthesized from titanium nitride: Characterizations and photocatalytic hydrogen evolution performance. *J. Adv. Oxid. Technol.* **2013**, *16*, 131–136. [CrossRef]
73. Tristantini, D.; Ibadurrohman, M. Photocatalytic hydrogen production from glycerol–water mixture over Pt-N-TiO_2 nanotube photocatalyst. *Int. J. Energy Res.* **2013**, *11*, 1372–1381.
74. Wei, X.; Li, J.; Liu, Z.; Yang, X.; Naraginti, S.; Xu, X.; Wang, X. Visible light photocatalytic mineralization of 17α-ethinyl estradiol (EE2) and hydrogen evolution over silver and strontium modified TiO_2 nanoparticles: Mechanisms and phytotoxicity assessment. *RSC Adv.* **2018**, *8*, 4329–4339. [CrossRef]
75. Chen, D.; Gao, H.; Yao, Y.; Zhu, L.; Zhou, X.; Peng, X.; Zhang, X. Pd loading, Mn+ (n= 1, 2, 3) metal ions doped TiO_2 nanosheets for enhanced photocatalytic H_2 production and reaction mechanism. *Int. J. Hydrog. Energy* **2022**, *47*, 10250–10260. [CrossRef]

76. Nguyen, C.; Dinh, C.; Do, T. Hollow Sr/Rh-codoped TiO_2 photocatalyst for efficient sunlight-driven organic compound degradation. *RSC Adv.* **2017**, *7*, 3480–3487. [CrossRef]
77. Li, C.; Hu, P.; Meng, H.; Jiang, Z. Role of sulfites in the water splitting reaction. *J. Sol. Chem.* **2016**, *45*, 67–80. [CrossRef]
78. Chandra, M.; Bhunia, K.; Pradhan, D. Controlled synthesis of CuS/TiO_2 heterostructured nanocomposites for enhanced photocatalytic hydrogen generation through water splitting. *Inorg. Chem.* **2018**, *57*, 4524–4533. [CrossRef]
79. da Silva, G.C.; Venturini, S.I.; Zhang, S.; Löffler, M.; Scheu, C.; Mayrhofer, K.J.; Ticianelli, E.A.; Cherevko, S. Oxygen evolution reaction on tin oxides supported iridium catalysts: Do we need dopants? *ChemElectroChem* **2020**, *7*, 2330–2339. [CrossRef]
80. Phul, R.; Perwez, M.; Ahmed, J.; Sardar, M.; Alshehri, S.M.; Alhokbany, N.; Khan, M.A.A.; Ahmad, T. Efficient multifunctional catalytic and sensing properties of synthesized ruthenium oxide nanoparticles. *Catalysts* **2020**, *10*, 780. [CrossRef]